Accepted Manuscript

Title: Structural and mechanical properties of nanocrystalline Zr co-sputtered a-C(:H) amorphous films

Author: A. Escudeiro N.M Figueiredo T. Polcar A. Cavaleiro

PII: S0169-4332(14)02470-2
DOI: http://dx.doi.org/doi:10.1016/j.apsusc.2014.11.015
Reference: APSUSC 29060

To appear in: *APSUSC*

Received date: 28-8-2014
Revised date: 3-11-2014
Accepted date: 3-11-2014

Please cite this article as: A. Escudeiro, N.M. Figueiredo, T. Polcar, A. Cavaleiro, Structural and mechanical properties of nanocrystalline Zr co-sputtered a-C(:H) amorphous films, *Applied Surface Science* (2014), http://dx.doi.org/10.1016/j.apsusc.2014.11.015

Structural and mechanical properties of nanocrystalline Zr co-sputtered a-C(:H) amorphous films

A. Escudeiro[1], N.M Figueiredo[1], T. Polcar[2,3] and A. Cavaleiro[1]

[1]SEG-CEMUC DEM University of Coimbra, Coimbra, Portugal
[2]Engineering Materials, Faculty of Engineering and the Environment, University of Southampton, SO17 1BJ, United Kingdom
[3]Department of Control Engineering, Czech Technical University in Prague, Technicka 2, Prague 6, Czech Republic

Abstract:

The aim of this study was to investigate the effect of Zr as alloying element to carbon films, particularly in respect to film structure and mechanical properties. The films were deposited by magnetron sputtering in reactive (Ar+CH_4) and non-reactive (Ar) atmosphere with different Zr contents (from 0 to 14 at.%) in order to achieve a nanocomposite based films. With an increase of Zr content a broad peak was observed in X-ray diffraction spectra suggesting the presence of nanocrystalline (nc) ZrC phase for the coatings with Zr content higher than 4 at.%. The application of Scherrer formula yielded a grain sizes with a dimension of 1.0-2.2 nm. These results were supported by X-ray photoelectron spectroscopy showing typical charge transfer at Zr-C nanograins and carbon matrix interface. The nc-ZrC phase was also observed by transmission electron microscopy. The hardness of the coatings was approximately independent of Zr content. However, the Young modulus increased linearly. The residual stress of the coatings was strongly improved by the presence of nc-ZrC phase embedded in the a-C matrix. Finally, the incorporation of H into the matrix led to denser and harder films.

1. Introduction

Diamond-like carbon (DLC) coatings are considered an attractive protective surface treatment which combines high hardness and wear resistance with low coefficient of friction, helping to reduce friction losses and to increase load carrying capacity. At the same time, hard DLC coatings are generally characterized by high compressive stress which limits their adhesion to the metallic substrate and makes them brittle under the applied loading. Fortunately, their doping or alloying with non-metallic (N, H, O) and/or metallic (Ti, Cr, W, Ag) elements helps to relax the amorphous carbon (a-C) network by forming a nanocomposite structure [1-4]. Moreover, transition metal-carbides show unique combination of materials of solid-state properties such as very high hardness and excellent electrical and thermal conductivity [5]. If transition metals are introduced into the carbon matrix above a certain concentration, nanocrystalline (nc) particles are formed acting as a reinforcing phase. In fact, Meng et al [6, 7] reported a maximum limit of dissolution of Ti atoms into an a-C:H (hydrogenated) matrix between 0.9 and 2.5 at.% and for a-C matrix between 4 and 8 at.%; for higher Ti concentration, nanocomposite materials could be formed. Mechanical, thermal and electrical properties of the coatings can be then enhanced controlling the size and the volume fraction of the nc-phase [8, 9]. Voevodin and co-workers pioneered nanostructured materials [10, 11]. For instance, when alloying with Ti, the TiC/DLC systems exhibit a large amount of grain boundaries between the nc-TiC phase and the amorphous DLC matrix, which effectively enhances the hardness and toughness of the coatings, limiting crack initiation and/or terminating further crack growth and film delamination [8-10, 12-14]. Moreover, such nanocomposite structure could also lower the friction and wear and significantly improve load carrying capacity [11]. Apparently, encapsulation of finer grains of hard nc-TiC within the amorphous DLC matrix restricts dislocation activity, diverts and arrests macrocracks development, and maintains the high level of hardness [9, 13]. The interface between both phases also plays an important role, since interfacial fraction in nanocomposites is very high [15]. It was found that the charge transfer from the Ti 3d to C 2p orbitals may contribute to the mechanical stability of the material by enhancing the inter-phase bonding [15-17]. Therefore, nanocomposite coatings are expected to have high hardness and fracture toughness since the carbide crystals are small and help to block (micro-)crack propagation together with the amorphous carbon phase which provides self-lubrication properties [8, 9, 13, 18, 19].

In this study, Zr, as a strong carbide forming element, was chosen as doping element and incorporated into amorphous carbon matrix in order to form nanocomposite

coatings. Coating microstructure is studied in detail and related with mechanical properties.

2. Materials and Experimental Details

2.1 Coatings deposition

The coatings were deposited using dc magnetron sputtering under reactive (Ar + CH_4) and non-reactive atmosphere (Ar) in order to deposit hydrogenated and non-hydrogenated coatings, respectively. Two targets were used: Ti, to deposit the gradient interface layer (Ti/TiN/TiCN), and graphite, to deposit the functional coating. Zr-containing films were produced through the incorporation of Zr pellets into the erosion area of the graphite target (see table 1). Prior to deposition the substrates (Si wafers, mirror polished thin 304 SS and M2 steel discs) were ultrasonic cleaned in acetone, alcohol and distilled water. The substrates were then placed into the vacuum chamber and sputtered etched, via Ar^+ bombardment (-650V bias voltage), for cleaning any additional oxides and surface contaminants. The Ti-based gradient layer (~650 nm) was then deposited in order to improve adhesion. The deposition parameters were maintained constant for all depositions: 7.5 $W.cm^{-2}$ target power density, total pressure 0.4 Pa, sample rotation 18 rpm, bias voltage applied to substrates -50 V. In order to produce hydrogenated coatings, CH_4 was introduced into the deposition chamber while the number of Zr pellets was maintained. The Ar/CH_4 flux was adjusted in order to maintain the total pressure constant. The deposition time was set to deposit coatings approximately 1.6 μm thick. Further deposition details can be found elsewhere [20]. To facilitate reading, the coatings were denominated as a-C_Zr(X) and a-C:H_Zr(X) for non-hydrogenated and hydrogenated coatings, respectively, where X is the approximate Zr content.

2.2 Microstructure, composition and morphology

The phase identification was performed using synchrotron radiation at the Materials Research station of the Rossendorf beam line (ROBL-MRH) located at the bending magnet 20 (BM20) at the European Synchrotron Radiation Facility (ESRF) in Grenoble. The incident X-ray beam was monochromatized to an energy of 11.5 keV (λ = 0.1078 nm). To increase the signal from the coating and in order to identify any crystalline phase, grazing angle incidence X-ray diffraction was performed; hereby the sample surface was tilted 2º in relation to the synchrotron beam. The chemical bonding of the films was evaluated by XPS analysis using a Kratos AXIS Ultra HSA, with VISION

software for data acquisition. The analysis was carried out with a monochromatic Al Kα X-ray source (1486.7 eV), operating at 15kV (90 W), in FAT mode (Fixed Analyser Transmission), with a pass energy of 40 eV for regions ROI and 80 eV for survey. Data acquisition was performed at a pressure lower than 1 x 10^{-6} Pa and charge neutralisation system was used. The samples were sputter-cleaned with Ar^+ ion gun (4 keV) prior to spectra acquisition (30 min) in order to remove any residual contamination, corresponding to a sputter depth of 0.01 nm/min (~0.3 nm). The modeling of the spectra was performed using the CasaXPS program, in which an adjustment of the peaks was performed using peak fitting with Gaussian-Lorentzian peak shape and Shirley type background subtraction. The charging effects were corrected at the surface by assuming C-C bond binding energy (BE) at 285 eV in the C 1s spectrum. For the deconvolution of Zr 3d peaks the spin-orbital splitting was assumed to be constant for all phases (2.4 eV) and the integrated area relatively to that of the Zr $3d_{5/2}$ peak was considered as equal to the spin-orbit multiplicity of 2/3 [21]. The chemical composition was also evaluated by XPS from the relative peak intensity, corrected by experimentally determined sensitivity factors.

The surface morphology and cross-section of the coatings were investigated using a scanning electron microscope (SEM, FEI Quanta 400FEG E SEM – EDAX Genesis X4M) and atomic force microscopy (AFM, AFM – Bruker Innova). The average roughness (Ra) was evaluated by AFM on a 5 µm x 5 µm line scan. The investigation of the nanostructure was carried out by transmission electron microscopy (TEM) with a FEI Tecnai G2 T20 microscope with a LaB_6 filament operated at 200 kV and a FEI Titan 80-300 microscope equipped with field emission gun (FEG) and Gatan image filter (GIF) Tridium and operated at 300kV. Both bright field (BF) imaging and selected area electron diffraction (SAED) were carried out. SAED was performed with an aperture size of ~ 100 nm in diameter. TEM specimens were prepared using an FEI Versa3D focus ion beam – scanning electron microscope (FIB-SEM).

2.3 Mechanical properties

The hardness of the coatings was evaluated by depth-sensing indentation (Micromaterials Nanotest) using a Berkovich indenter. The normal stylus load was 5 mN (indentation depth approx. 150 nm); 32 indentations from 2 distinct areas on the sample were carried out to evaluate hardness. Moreover, the reduced Young modulus was derived from the indentation measurements by standard Oliver and Pharr method [22]. The residual stress was calculated using the corrected Stoney equation [23] by

measuring the curvature of the SS304 thin disc substrate radii by 2D profilometer (Perthometer S4P) before and after coating deposition.

3. Results and Discussion:

3.1. Coating deposition and microstructure

Table 1 summarizes the deposition parameters and the corresponding chemical composition of the films (H excluded). The increase of the number of Zr pellets led to higher Zr content in the coatings and, consequently, the deposition rate also increased due to the higher sputtering rate of Zr in relation to C [20, 24]. The introduction of CH_4 further increased the deposition rate; however, Zr content was lower due to the presence of a second C source. The oxygen contamination originated from the chamber atmosphere was very low (2 at.% data from EDX). The oxygen content measured by XPS was found to be dependent on the Zr content (see Table 1). Prior to XPS signal acquisition, the surfaces were sputter-clean by ion bombardment to clean the surface from contamination. For high Zr contents (14 at.%), the presence of oxygen was detected even after very long ion bombardment (40 min). We assume that the increase of metal/carbon ratio caused by preferential sputtering led to a higher oxygen adsorption and the generation of oxide films on the exposed ZrC nanocrystallines, as will be discuss later [25-27].

The SEM micrographs presented in Figure 1 show fractured cross-section of selected coatings. The columnar intermediate layer (Ti/TiN/TiCN) is visible between substrate and functional top coating. The same morphology was observed when TiN was deposited by reactive magnetron sputtering at low temperature and low bias voltage [28, 29]. a-C films revealed a columnar morphology, which led to a cauliflower-like patterned surface resulting from the shadow effects and low adatom mobility (see Figure 2). Columnar growth is commonly associated with growth defects and low toughness coatings which may led to crack initiation/propagation through the columnar boundaries after high load contact [9]. The incorporation of Zr did not produce any significant morphological change; however, the films became denser and smoother. In our previous study, we found that the density was higher with the increase of Zr content. Figure 3 shows a TEM BF image from the interface between adhesion interlayer and a-C_Zr(14) functional coating. The pronounced columnar structure from the Ti-based interlayer quickly transforms to a rather featureless structure, where only thin and discontinuous columnar boundaries can be seen along the coating growth direction. The presence of heavier atoms, such as Zr, causes preferential growth of ZrC islands while carbon, as lighter atom with expected higher mobility, will be knocked-down to fill the

voids reaching the shadowing portions of the coatings and thus promoting the structure rearrangement [13]. The introduction of CH_4 enhances the compact microstructure and eliminated the columnar structure of the films due to two factors: (i) the incorporation of H in the carbon coatings prevent formation of the column boundaries due to high mobility of hydrocarbon species [14] and (ii) a quick fill up of the shadowed areas, since the carbonaceous phases can land from any angle smoothing the growing interface and thus restraining the columnar growth [13].

3.2. Structure and chemical bonding

Figure 4 shows the X-ray diffractograms of the alloyed non-hydrogenated films. The presence of Si, Ti and TiN peaks originated in a graded Ti/TiN/TiCN interlayer and Si substrate. With the increase of Zr content, a broad peak appeared at ZrC phase position (ICDD card no. 74-1221). The presence of broad peaks is common in nanocomposite and nanostructured films, where the limited size of the diffracting crystals causes broadening of the peak. The peaks were fitted using a pseudo-Voigt function (see Figure 4 inset) and by fixing the position the interlayer correspondent peaks and allowing the background and the position areas of ZrC peaks to vary. For low Zr content (4 at.%), the deconvolution was found to be very difficult due to the extremely low intensity peak. The particle size estimated by the Scherrer formula [30] slightly increased from 1.0 to 2.2 nm for Zr content 4 and 14 at.%, respectively. The same was observed for the hydrogenated coating (not shown). Raman spectra was used to characterized the amorphous C-matrix. The incorporation of Zr and H led to the formation of aromatic rings and the organization and size of the C-clusters in the C-matrix as seen in our previous study [20].

TEM investigations were performed on selected samples to verify the XRD results. Figure 5 shows the TEM micrographs and the schematic representation of the particle distribution of a-C_Zr(14) and a-C_Zr(4). The schematic representation was obtained by using the Mathematica software to model the particle distribution taking into consideration the nanoparticle volume fraction (V_F) and the ZrC nanoparticles size for a unit cell of 20 x 20 x 5 nm^3. TEM of a-C_Zr(14) coating clearly shows ~2nm nanocrystalline ZrC grains randomly distributed in an amorphous carbon matrix (see Figure 5a). Other smaller nanoparticles are also expected to be present; however, their very small size (< 1.5 nm) makes them almost imperceptible to the BF TEM. For a-C_Zr(4) coating (see Figure 5b) only smaller nanoparticles are expected to be dispersed in the a-C matrix. Again, such small sizes (< 1 nm) should be rather difficult to identify in TEM micrographs. Fast Fourier transform (FFT) analysis of the a-C_Zr(14) revealed sharp and discrete rings between the lattice planes corresponding to that of ZrC (not

shown). Using the model, the average inter-particle distance was found to be around 9 nm, irrespectively of the Zr content. Thus, in all cases the separation of ZrC nanograins by an amorphous carbon phase is high enough (>> particle size) to isolate the nanoparticles effectively and limits the grain growth via diffusion and coalescence [31].

Information about the chemical state and chemical environment of C and Zr in the coatings was evaluated by XPS. Figure 6 shows the core-level spectra of the analyzed elements: C 1s, Zr 3d and O 1s after Ar^+ sputter cleaning. Table 2 and 3 show, respectively, the relevant BE found in literature and the experimental BE values obtained after fitting the XPS spectra according to the different types of bonds expected in the coatings.

Figure 6a shows the carbon C 1s spectral fitting for non-hydrogenated samples. The carbon peak was fitted using the main peak (285 eV) ascribed as alkyl type carbon (C-C, C-H). A second peak was added (286.3 eV) with the same FWHM as the main peak ascribing the alcohol (C-OH) and/or ester (C-O-C) functionality. Two other components were also added corresponding to the C=O and O-C=O at 287.8 eV and 289.3 eV, respectively. When Zr was incorporated in the matrix an extra peak appeared with BE close to 283.5±0.1 eV (see Table 3). The position of this peak (BE value) stayed approximately constant with Zr content in the films. A peak between typical C-Me and C-C bonds has been reported by many authors for nc-MeC/a-C systems (Me = Zr, Ti and Nb) [15-17, 31, 38, 42]; it was suggested to originate from an interfacial state at the carbide and amorphous matrix interface (Me-C*). The presence of nanocrystallites can enhance the charge transfer between the positive metal element and the C-matrix through adsorption of stable building units of a-C(:H) (e.g. extended sp^2-bonded islands with their stabilizing π-system) [42, 44]. In fact, Magnuson et. al. [17] suggested that, for nc-TiC/a-C films, electron transfer occurs between Ti 3d and C 2p. The electron deficiency, caused by such net charge transfer from Ti to the C-matrix, can be then spread out across the entire carbide grain [17, 45]. For larger grains such deficiency is negligible; however, for nanograins the electron deficiency will weaken the Me-C bond within carbide. These interface regions were predicted to be around 1 nm thick [16]. A higher total charge transfer from the Zr nearest neighbours to interfacial C atoms is expected leading to higher chemical shift [42, 45]. Thus, for the present case, the ZrC bonds are expected to be characteristic of small ZrC nanoparticles (C-Zr*).

Zr 3d spectra are shown in Figure 6c. The Zr metallic phase (178.0-179.1 eV) was not observed in any sample. Likewise in the C 1s spectra, Zr 3d peak also shifts approximately 1.0 eV to HBE when compared to typical ZrC peak of a bulk material (179.9 ± 1.8 eV). Many authors [38, 44, 46, 47] reported similar shifts for small grain sizes. Contrarily to the C 1s, for the Zr 3d case it was observed a reduction of the BE

shift with increasing Zr content (Figure 6c and Table 2). For smaller cluster sizes the electron deficiency in Zr atoms is expected to be higher, leading to HBE shifts [45].

The presence of Zr-O bonds in the Zr 3d spectra (182.4 eV) was also observed, even after ion bombardment. Despite the low oxygen content in the film, the O-Zr contribution in the Zr 3d spectra was around 50% for higher Zr contents. The ion bombardment may induce carbon preferential sputtering causing ZrC nanocrystals exposure to the environment resulting in ZrO_2 formation [27]. Zr is easily oxidized (ZrO_2) showing its high ability to passivate, which might be a beneficial property for corrosion resistance. These bonds were also confirmed in O 1s range of energies revealing a peak at 531.2 eV previously reported as Zr-O bond (Figure 6b).

3.4. Mechanical properties

DLC films are known to have high compressive residual stress due to their peculiar amorphous structure (> 3GPa) [48]. Table 4 shows the compressive residual stress for Zr-free and Zr-containing films. In our case, thermal mismatch is minimized since magnetron sputtering is characterized by a low deposition temperature [49] and no external heating was used. Furthermore, the use of graded layers (Ti/TiN/TiNC) helped to decrease the abrupt composition changes between the film and the substrate and thus decreasing the residual stress and improving the adhesion. The intrinsic stress was strongly dependent on the chemical composition, morphology and microstructure of the films. The incorporation of Zr relaxed the stresses in the films: the higher the Zr content, the lower the stress is. Zr acted as a catalyst forming a nanophase of ZrC and reacting with the C-matrix by overlapping Zr d-orbitals with C p-orbitals. The break of the C bonds may release the stress through the formation of a more graphite-like film as seen in our previous study [20]. The same tendency was also observed by Zou et al [50] for DLC coatings doped with low Cr contents. On the other hand, simultaneous incorporation of both H and Zr did not promote such relaxation. The presence of a reactive gas (CH_4) enhanced the bombardment of the film by the hydrocarbon species and their consequent penetration in the structure. Thus, a denser network structure was formed (see section 3.1) which led to an increase in the residual stress [13, 48].

The presence of ZrC nanograins did not significantly change the hardness of the coatings compared to Zr-free ones. The hardness of nanocomposite films is typically influenced by the size, orientation and shape of the embedded nanograins [11]. For hard coatings the key challenge is to avoid grain boundary sliding leaving the grain rotation as the deformation mechanism: small interparticle separation (few atomic layers) and higher volume fraction (V_F) of nano particles (3-5 nm) is required. On the other hand, toughness is achieved by larger interparticle separation and thus, lower V_F, which allows shear delocalization [11, 44, 51]. Since small nanograins of ZrC (< 3 nm) were

separated by a thick carbon layer (see Section 3.2) the classical Hall-Petch effect can not be considered; moreover, two factors contribution to high hardness could be well balanced in our system – higher amount of carbides results in lower compressive stress, so the final hardness could be almost identical for different Zr contents and similar to pure carbon films. On the other hand, the Young modulus increased with the increase of Zr-content (see Table 4), since the embedded ZrC phase presents higher elastic modulus compared to a-C matrix [5].

Other important parameters for hard coatings are H/E and H^3/E^2 which are closely related to the wear resistance and the plastic behavior under Hertzian contact, respectively [52]. Since the hardness was almost independent of Zr content, both parameters slightly decreased with the increase of Zr content. The methane flux during the deposition resulted in an increase of H/E and H^3/E^2 when compared to non-hydrogenated films. As expected, the lack of columnar boundaries (i.e. glassy microstructure, see Figure 1) together with modified nature of carbon matrix by hydrogen led to slightly higher hardness value. The wear resistance is thus expected to be higher for Zr-containing hydrogenated samples.

Conclusion

The formation of nanocomposite structures consisting of ZrC nano-particles in an amorphous carbon matrix has been analysed in detail by SEM, XRD, XPS and TEM. The incorporation of 4 at.% of Zr resulted in the presence of ZrC nanophase embedded in a carbon matrix. The grain size estimated by XRD peak fitting and directly measured by TEM was between 1.0-2.5 nm. The presence of such nanophase ZrC was also confirmed by XPS where additional bonding states were identified due to the small grain size of the carbide phase. The interaction of ZrC with the matrix led to significant charge transfer, which shifted ZrC XPS peak to HBE. Mechanical properties were related to chemical bonding and coating microstructure. With the increase of Zr content the columnar microstructure of the coatings became featureless. The hardness was almost independent of Zr content; however, the change in Young modulus led to different H/E and H^3/E^2, which decreased with the increase of Zr content. Higher amount of Zr decreased residual stress. The introduction of the reactive gas into the chamber further enhanced the properties of the coatings. The high mobility of the hydrocarbon species led to a more compact/glassy microstructure, constraining the typical columnar microstructure and improving the mechanical properties.

Acknowledgment

This research was sponsored by FEDER funds through the program COMPETE – Programa Operacional Factores de Competitividade – and by national funds through FCT – Fundação para a Ciência e a Tecnologia –, under the project PEst-C/EME/UI0285/2011 and QREN-POPH for funding support under the grant SFRH/BD/75071/2010 which was co-funded by FSE and MSTES. The research has also received funding from the European Union Seventh Framework Programme under Grant Agreement 312483 – ESTEEM2 (Integrated Infrastructure Initiative – I3). The authors would like as well to thank André J. Cavaleiro from University of Coimbra, Portugal and C. Baehtz from Helmholtz-Zentrum Dresden-Rossendorf, Germany for performing and supporting the synchrotron radiation experiments, respectively. We also thank Lunjie Zeng from Chalmers University of Technology and Liliana Alves from CEMUP for TEM measurements and XPS analysis, respectively, and for all valuable discussions.

References:

[1] N. K. Manninen, F. Ribeiro, A. Escudeiro, T. Polcar, S. Carvalho, A. Cavaleiro, Influence of Ag content on mechanical and tribological behavior of DLC coatings, Surf. Coat. Tech. 232 (2013) 440-446.

[2] R. M. Balestra, A. M. G. Castro, M. Evaristo, A. Escudeiro, P. Mutafov, T. Polcar, A. Cavaleiro, Carbon-based coatings doped by copper: Tribological and mechanical behavior in olive oil lubrication, Surf. Coat. Tech. 205 (2011) S79-S83.

[3] C. W. Moura e Silva, J. R. T. Branco, A. Cavaleiro, How can H content influence the tribological behaviour of W-containing DLC coatings, Solid State Sci. 11 (2009) 1778-1782.

[4] J. C. Sánchez-López, A. Fernández, Doping and Alloying Effects on DLC Coatings, in: C. Donnet, A. Erdemir (Eds.), Tribology of Diamond-Like Carbon Films, Springer US, 2008, pp. 311-338.

[5] W. Lengauer, A. Eder, Carbides: Transition Metal Solid-State Chemistry, in Encyclopedia of Inorganic Chemistry, ed: John Wiley & Sons, Ltd, 2006.

[6] W. J. Meng, R. C. Tittsworth, L. E. Rehn, Mechanical properties and microstructure of TiC/amorphous hydrocarbon nanocomposite coatings, Thin Solid Films 377–378 (2000) 222-232.

[7] B. Feng, D. M. Cao, W. J. Meng, J. Xu, R. C. Tittsworth, L. E. Rehn, et al., Characterization of microstructure and mechanical behavior of sputter deposited Ti-containing amorphous carbon coatings, Surf. Coat. Tech. 148 (2011) 153-162.

[8] Y. T. Pei, D. Galvan, J. T. M. De Hosson, C. Strondl, Advanced TiC/a-C:H nanocomposite coatings deposited by magnetron sputtering, J. Eur. Ceram. Soc. 26 (2006) 565-570.

[9] Y. T. Pei, D. Galvan, J. T. M. De Hosson, A. Cavaleiro, Nanostructured TiC/a-C coatings for low friction and wear resistant applications, Surf. Coat. Tech. 198 (2005) 44-50.

[10] A. Voevodin, S. Prasad, and J. Zabinski, "Nanocrystalline carbide/amorphous carbon composites," J Appl Phys, 82 (1997) 855-858.

[11] P. M. Martin, Handbook of Deposition Technologies for Films and Coatings: Science, Applications and Technology: Elsevier Science, 2009.

[12] A. Voevodin, M. Capano, S. Laube, M. Donley, and J. Zabinski, "Design of a Ti/TiC/DLC functionally gradient coating based on studies of structural transitions in Ti–C thin films" Thin Solid Films, 298 (1997) 107-115.

[13] Y. T. Pei, D. Galvan, and J. T. M. De Hosson, "Nanostructure and properties of TiC/a-C:H composite coatings" Acta Materialia 53 (2005) 4505-4521.

[14] Y. T. Pei, C. Q. Chen, K. P. Shaha, J. T. M. De Hosson, J. W. Bradley, S. A. Voronin, *et al.*, "Microstructural control of TiC/a-C nanocomposite coatings with pulsed magnetron sputtering" *Acta Materialia,* vol. 56, pp. 696-709, 2// 2008.

[15] U. Jansson, E. Lewin, Sputter deposition of transition-metal carbide films — A critical review from a chemical perspective, Thin Solid Films 536 (2013) 1-24.

[16] E. Lewin, P. O. Å. Persson, M. Lattemann, M. Stüber, M. Gorgoi, A. Sandell, et al., On the origin of a third spectral component of C1s XPS-spectra for nc-TiC/aC nanocomposite thin films, Surf. Coat. Tech. 202 (2008) 3563-3570.

[17] M. Magnuson, E. Lewin, L. Hultman, U. Jansson, Electronic structure and chemical bonding of nanocrystalline-TiC/amorphous-C nanocomposites, Phys. Rev. B 80 (2009) 235108.

[18] D. Martínez-Martínez, C. López-Cartes, A. Fernández, J. C. Sánchez-López, Influence of the microstructure on the mechanical and tribological behavior of TiC/a-C nanocomposite coatings, Thin Solid Films 517 (2009) 1662-1671.

[19] A. A. Voevodin, J. S. Zabinski, Supertough wear-resistant coatings with ‘chameleon’ surface adaptation, Thin Solid Films 370 (2000) 223-231.

[20] A. Escudeiro, T. Polcar, A. Cavaleiro, a-C(:H) and a-C(:H)_Zr coatings deposited on biomedical Ti-based substrates: Tribological properties, Thin Solid Films, 538 (2013) 89-96.

[21] C. D. Wagner, W. M. Riggs, L. E. Davis, J. F. Moulder, G. E. Muilenberg, Handbook of X-Ray Photoelectron Spectroscopy, Minnesota: Perkin-Elmer Corporation, 1979.

[22] W. C. Oliver, G. M. Pharr, An improved technique for determining hardness and elastic modulus using load and displacement sensing indentation experiments, J. Mater. Res. 7 (1992) 1564-1583.
[23] G. G. Stoney, The Tension of Metallic Films Deposited by Electrolysis, P. R. Soc. Lond. Ser.-A 82(1909) 172-175.
[24] A. Escudeiro, T. Polcar, A. Cavaleiro, Adsorption of bovine serum albumin on Zr co-sputtered a-C(:H) films: Implication on wear behaviour, J. Mech. Behav. Biomed. 39 (2014) 316-327.
[25] P. Frantz, S. V. Didziulis, Detailed spectroscopic studies of oxygen on metal carbide surfaces, Surf. Sci. 412–413 (1998) 384-396.
[26] J. A. Rodriguez, P. Liu, J. Gomes, K. Nakamura, F. Viñes, C. Sousa, et al., Interaction of oxygen with ZrC(001) and VC(001): Photoemission and first-principles studies, Phys. Rev. B 72 (2005) 075427.
[27] A. A. El Mel, B. Angleraud, E. Gautron, A. Granier, P. Y. Tessier, XPS study of the surface composition modification of nc-TiC/C nanocomposite films under in situ argon ion bombardment, Thin Solid Films 519 (2011) 3982-3985.
[28] F. Fernandes, A. Loureiro, T. Polcar, A. Cavaleiro, The effect of increasing V content on the structure, mechanical properties and oxidation resistance of Ti–Si–V–N films deposited by DC reactive magnetron sputtering, Appl. Surf. Sci. 289 (2014) 114-123.
[29] F. Vaz, P. Machado, L. Rebouta, J. A. Mendes, S. Lanceros-Méndez, L. Cunha, et al., Physical and morphological characterization of reactively magnetron sputtered TiN films, Thin Solid Films 420–421 (2002) 421-428.
[30] M. Birkholz, Line Profile Analysis, in Thin Film Analysis by X-Ray Scattering, ed: Wiley-VCH Verlag GmbH & Co. KGaA, 2006, pp. 85-141.
[31] W. Gulbiński, S. Mathur, H. Shen, T. Suszko, A. Gilewicz, B. Warcholiński, Evaluation of phase, composition, microstructure and properties in TiC/a-C:H thin films deposited by magnetron sputtering, Appl. Surf. Sci. 239 (2005) 302-310.
[32] C. Morant, J. M. Sanz, L. Galán, L. Soriano, F. Rueda, An XPS study of the interaction of oxygen with zirconium, Surf. Sci. 218 (1989) 331-345.
[33] Y. F. Zheng, D. Liu, X. L. Liu, L. Li, Enhanced corrosion resistance of Zr coating on biomedical TiNi alloy prepared by plasma immersion ion implantation and deposition, Appl. Surf. Sci. 255 (2008) 512-514.
[34] S. Calderon V., R. E. Galindo, N. Benito, C. Palacio, A. Cavaleiro, S. Carvalho, Ag + release inhibition from ZrCN–Ag coatings by surface agglomeration mechanism: structural characterization, J. Phys. D Appl. Phys. 46 (2013) 325303.
[35] Y. S. Won, Y. S. Kim, V. G. Varanasi, O. Kryliouk, T. J. Anderson, C. T. Sirimanne, et al., "Growth of ZrC thin films by aerosol-assisted MOCVD," Journal of Crystal Growth, vol. 304, pp. 324-332, 2007.

[36] R. Kaufmann, H. Klewe-Nebenius, H. Moers, G. Pfennig, H. Jenett, H. J. Ache, XPS studies of the thermal behaviour of passivated Zircaloy-4 surfaces, Surf. Interface Ana. 11 (1988) 502-509.

[37] M. Balaceanu, M. Braic, V. Braic, A. Vladescu, C. C. Negrila, Surface chemistry of plasma deposited ZrC hard coatings, J. Optoelectron. Adv. M. 7 (2005) 2557-2560.

[38] M. Andersson, S. Urbonaite, E. Lewin, U. Jansson, Magnetron sputtering of Zr–Si–C thin films, Thin Solid Films 520 (2012) 6375-6381.

[39] D. Craciun, G. Bourne, G. Socol, N. Stefan, G. Dorcioman, E. Lambers, et al., Characteristics of ZrC/ZrN and ZrC/TiN multilayers grown by pulsed laser deposition, Appl. Surf. Sci. 257 (2011) 5332-5336.

[40] H. Hantsche, High resolution XPS of organic polymers, the scienta ESCA300 database. By G. Beamson and D. Briggs, Wiley, Chichester 1992, pp. 295

[41] A. Schroeder, G. Francz, A. Bruinink, R. Hauert, J. Mayer, E. Wintermantel, "Titanium containing amorphous hydrogenated carbon films (a-C:H/Ti): surface analysis and evaluation of cellular reactions using bone marrow cell cultures in vitro, Biomaterials 21 (2000) 449-456.

[42] Q. N. Meng, M. Wen, F. Mao, N. Nedfors, U. Jansson, W. T. Zheng, Deposition and characterization of reactive magnetron sputtered zirconium carbide films, Surf. Coat. Tech. 232 (2013) 876-883.

[43] S. S. Premathilaka, M. M. Hyland, Z. D. Chen, L. R. Watkins, B. Bansal, Interaction of whey protein with modified stainless steel surfaces, presented at the Proceedings of 7th International Conference on Heat Exchanger Fouling and Cleaning - Challenges and Opportunities, Tomar, Portugal, 2007.

[44] T. Zehnder, J. Patscheider, Nanocomposite TiC/a–C:H hard coatings deposited by reactive PVD, Surf. Coat. Tech. 133–134 (2000) 138-144.

[45] E. Lewin, M. Råsander, M. Klintenberg, A. Bergman, O. Eriksson, U. Jansson, Design of the lattice parameter of embedded nanoparticles," Chem. Phys. Lett. 496 (2010) 95-99.

[46] A. Nakao, M. Iwaki, J. Takahashi, K. Terashima, X-ray photoelectron spectroscopy study of zirconium-implanted iron and carbon-implanted zirconium, Surf. Coat. Tech. 66 (1994) 373-376.

[47] K. H. T. Raman, M. S. R. N. Kiran, U. Ramamurty, G. M. Rao, Structure and mechanical properties of TiC films deposited using combination of pulsed DC and normal DC magnetron co-sputtering, Appl. Surf. Sci. 258 (2012) 8629-8635.

[48] X. L. Peng, T. W. Clyne, Residual stress and debonding of DLC films on metallic substrates, Diam. Relat. Mat. 7 (1998) 944-950.

[49] Y. Pauleau, Residual Stresses in DLC Films and Adhesion to Various Substrates, in: C. Donnet, A. Erdemir (Eds.) Tribology of Diamond-Like Carbon Films, ed: Springer US, 2008, pp. 102-136.

[50] C. W. Zou, H. J. Wang, L. Feng, S. W. Xue, Effects of Cr concentrations on the microstructure, hardness, and temperature-dependent tribological properties of Cr-DLC coatings, Appl. Surf. Sci. 286 (2013) 137-141.
[51] T. Polcar, T. Vitu, L. Cvrcek, R. Novak, J. Vyskocil, A. Cavaleiro, Tribological behaviour of nanostructured Ti-C:H coatings for biomedical applications, Solid State Sci. 11 (2009) 1757-1761.
[52] A. Leyland, A. Matthews, On the significance of the H/E ratio in wear control: a nanocomposite coating approach to optimised tribological behaviour, Wear 246 (2000) 1-11.

Sample	A_{Zr}/A_C (%)	[O] (at.%)	[C] (at. %)	[Zr] (at. %)	Dep rate ($nm.s^{-1}$)	t (μm)	Ra [nm]
a-C	-	1	99	**-**	7.9	1.7	13.4±1
a-C_Zr(4)	2	2	94	**4**	8.4	1.7	7.3±1
a-C_Zr(7)	3	4	89	**7**	10.5	1.5	5.9±1
a-C_Zr(14)	6	8	78	**14**	11.4	1.5	5.8±1
a-C:H_Zr(10)*	6	3	87	**10**	13.2	1.6	4.4±1

* - Chemical composition not considering H content; H ~30 at.% [24]

Bond type	Spectra	Referenced BE (eV)	FWHM (eV)	Ref.
Zr (metal)	Zr $3d_{5/2}$	178.5	1.8	[32]
		178-179.1	-	[21, 33]
Zr-C	Zr $3d_{5/2}$	179.8	~1.2	[34]
		181.1	~ 2	[35]
		178.6-180.2	-	[33, 36-39]
Zr-O (Zr^{4+})	Zr $3d_{5/2}$	182.3-182.4	~2.6	[34]
		185.1	~2.5	[35]
		182.9 (Zr^{4+})	1.8	[32]
		181.9-183	-	[21, 33, 37]
C-C	C 1s	284.2-285	-	[21, 37, 40, 41]
C-O-C, C-OH	C 1s	285-286.5	-	[21, 37, 40, 41]
C=O	C 1s	287.8-288	-	[21, 37, 40]
O-C=O	C 1s	288.6-289.3	-	[37, 40, 41]
Zr-C	C 1s	282.5	~2	[34]
		282.9	~1.5	[35]
		281.7-282.3	-	[33, 36-38]
Zr-C*	C 1s	282.6-283.3	-	[20, 38, 42]
OAds	O 1s	531.9	-	[37]
		531.5	2.2	[41]
Zr-O	O 1s	531.2	1.7	[32]
		530.2-530.6	-	[21, 33, 37]
C-O, C=O, O-C=O (carbonyl)	O 1s	533.2-533.6	-	[41]
		532.4-532.7		[34, 43]

Sample	Spectra	C-C		C-O, C=O, O-C=O (carbonyl)		Zr-C		Zr-O ($Zr_{5/2}$)		O (adsorbed moisture)	
		BE (eV)	FWHM (eV)	BE (eV)	FWHM (eV)	BE (eV)	FWHM (eV)	BE (eV)	FWHM (eV)	BE (eV)	FWHM (eV)
DLC	C 1s	285.0	1.3	286.3	1.3	-	-				
				287.8	1.0						
				289.3	2.0						
	O 1s			533.6	2.3			-	-	531.8	2.4
DLC_Zr(4)	C 1s	285.0	1.4	286.3	1.4	283.4	1.0				
				287.8	1.4						
				289.3	2.0						
	O 1s			532.3	2.5			531.2	1.4	-	-
	Zr 3d					181.2	1.2	182.4	3.1		
DLC_Zr(7)	C 1s	285.0	1.4	286.3	1.4	283.6	1.1				
				287.8	1.3						
				289.3	2.0						
	O 1s			532.4	2.7			531.2	1.4	-	-
	Zr $3d_{5/2}$					181.0	1.3	182.4	2.9		
DLC_Zr(12)	C 1s	285.0	1.3	286.4	1.3	283.6	1.4				
				287.8	1.4						
				289.3	2.0						
	O 1s			532.3	2.5			531.2	1.3	-	-
	Zr $3d_{5/2}$					180.8	1.3	182.4	2.8		
DLC:H_Zr(8)	C 1s	285.0	1.4	286.3	1.4	283.6	1.3				
				287.8	1.5						
				289.3	2.0						
	O 1s			532.4	2.8			531.2	1.5	-	-
	Zr $3d_{5/2}$					180.7	1.2	182.4	2.6		

Samples	$\sigma_{compressive}$ [GPa]	*H* [GPa]	E [GPa]	*H*/E	H^3/E^2 [GPa]
a-C	1.9±0.6	11.2±0.6	110.4±6.5	0.10	0.12
a-C_Zr(4)	1.6±0.3	11.7±0.5	118.2±0.9	0.10	0.12
a-C_Zr(7)	1.0±0.6	11.4±0.6	126.6±4.4	0.09	0.09
a-C_Zr(13)	0.3±0.1	11.9±0.5	137.2±1.6	0.09	0.09
a-C:H_Zr(10)	1.7±0.4	12.7±0.6	120.2±1.0	0.11	0.14

Highlights:

- The incorporation of Zr led to formation of nanocrystalline ZrC embedded into C-matrix
- The incorporation of Zr and H decreased the typical columnar microstructure of a-C films.
- The hardness was independent on Zr content but increased with the introduction of H.

Figure

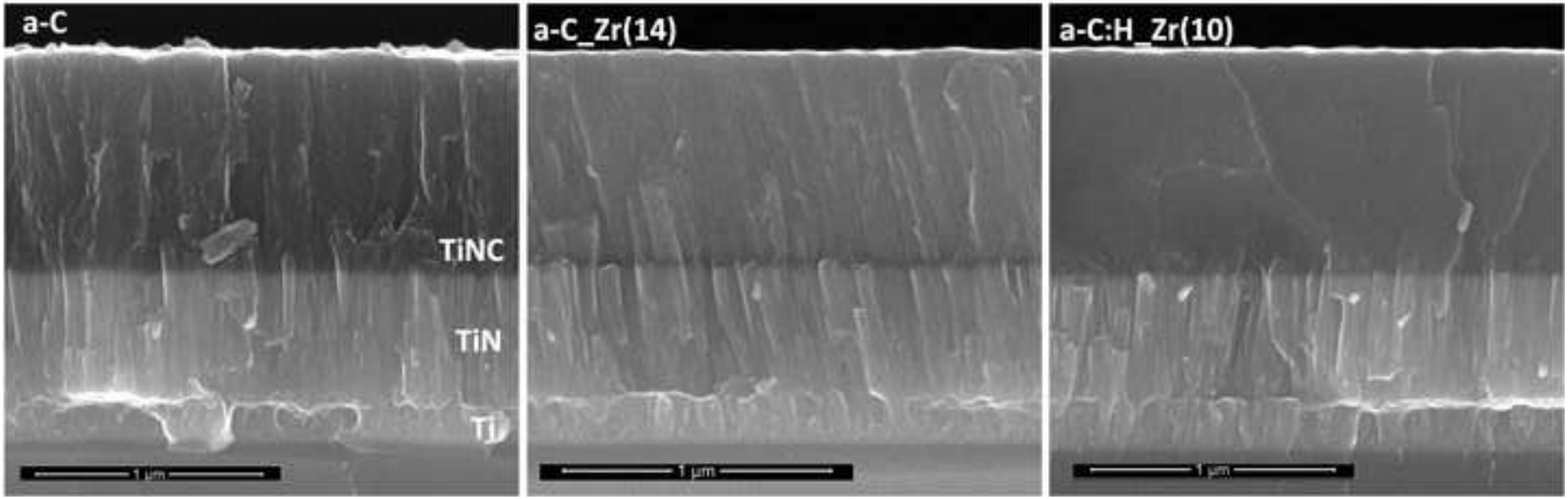

Figure2

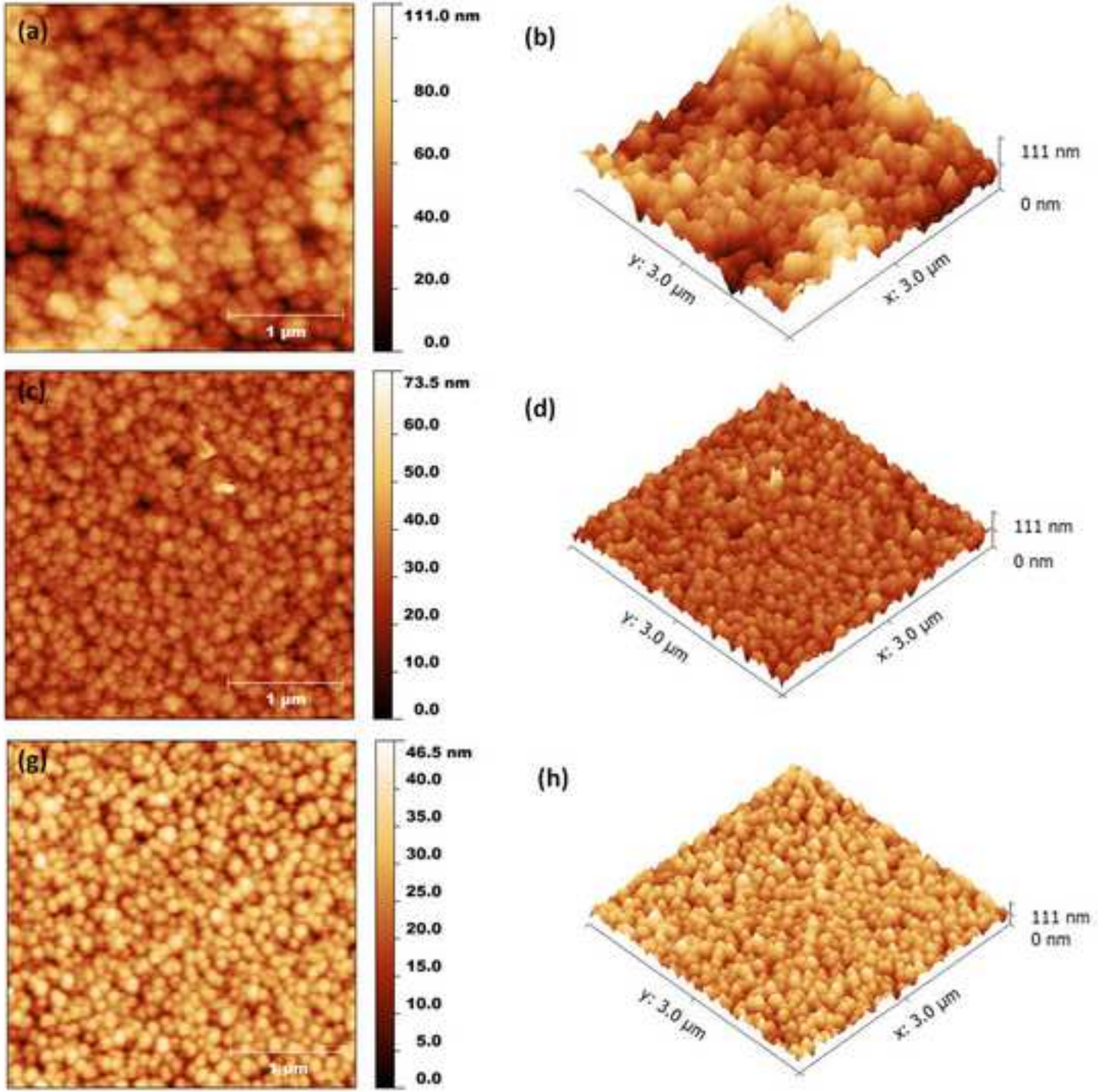
(a)
111.0 nm
80.0
60.0
40.0
20.0
0.0
1 µm
(b)
111 nm
0 nm
y: 3.0 µm
x: 3.0 µm
(c)
73.5 nm
60.0
50.0
40.0
30.0
20.0
10.0
0.0
1 µm
(d)
111 nm
0 nm
y: 3.0 µm
x: 3.0 µm
(g)
46.5 nm
40.0
35.0
30.0
25.0
20.0
15.0
10.0
5.0
0.0
1 µm
(h)
111 nm
0 nm
y: 3.0 µm
x: 3.0 µm

Figure3

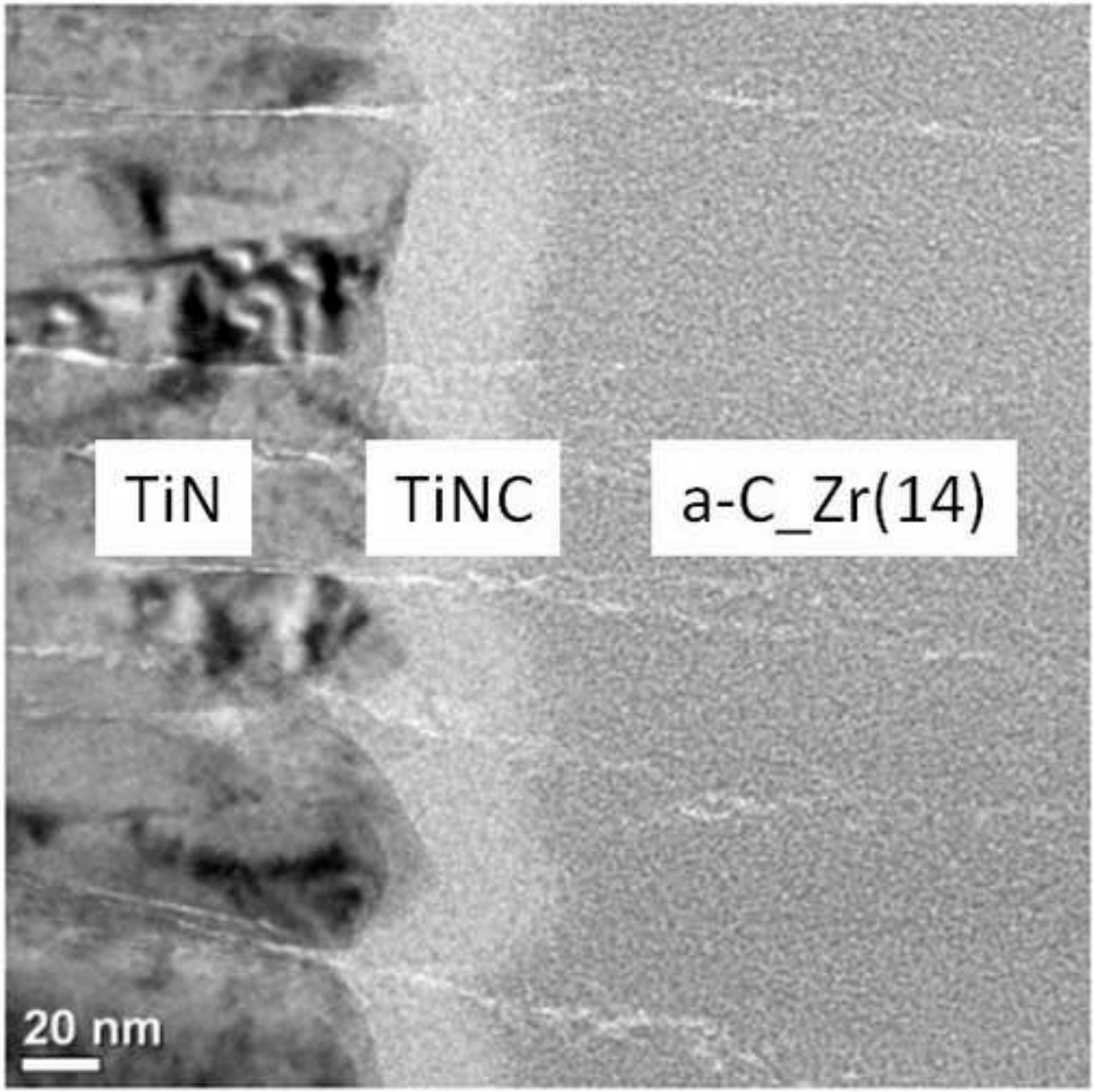

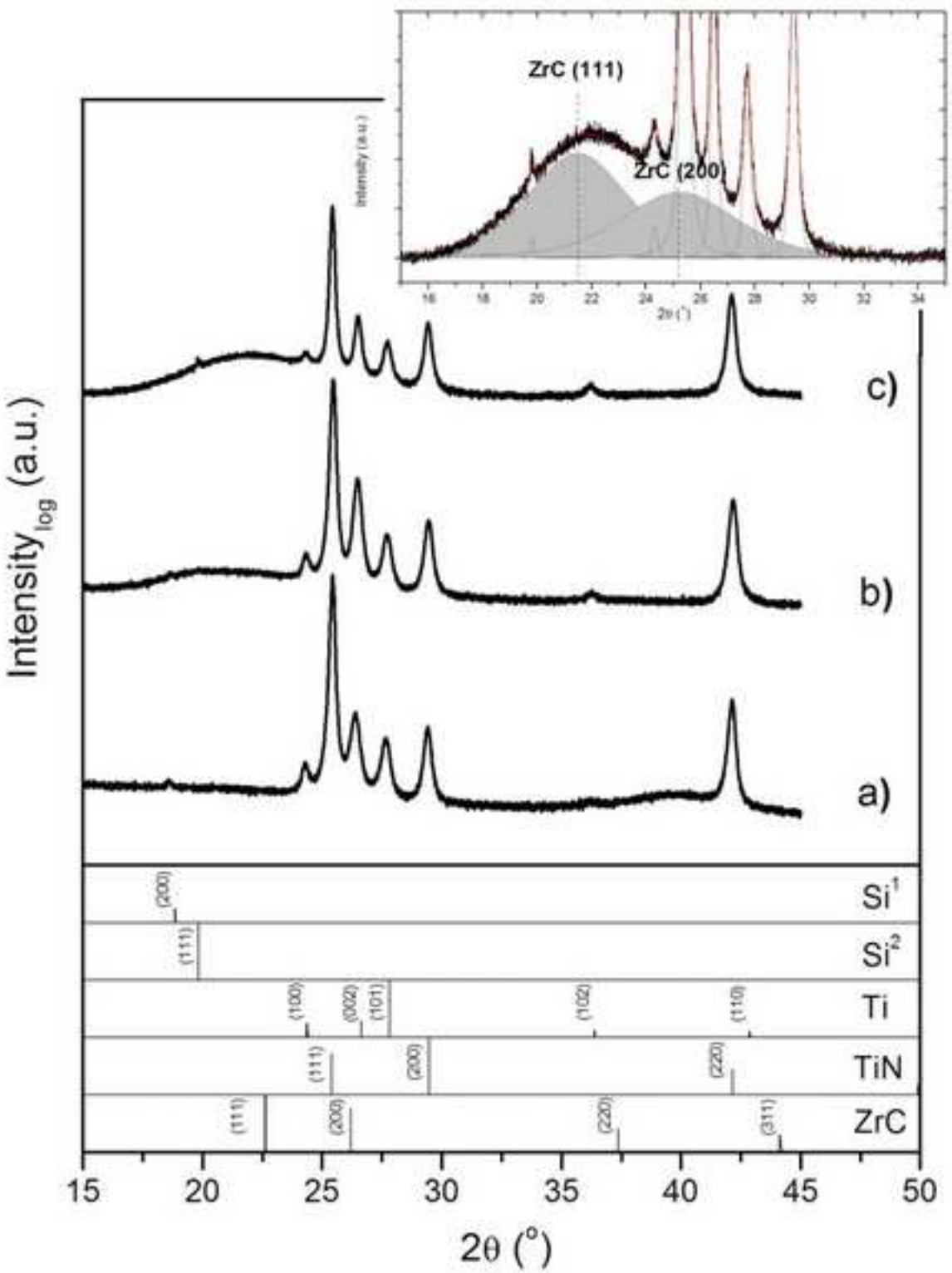

(a) a-C_Zr(14)

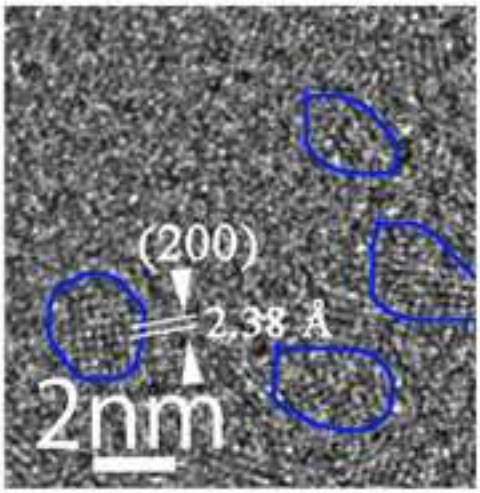

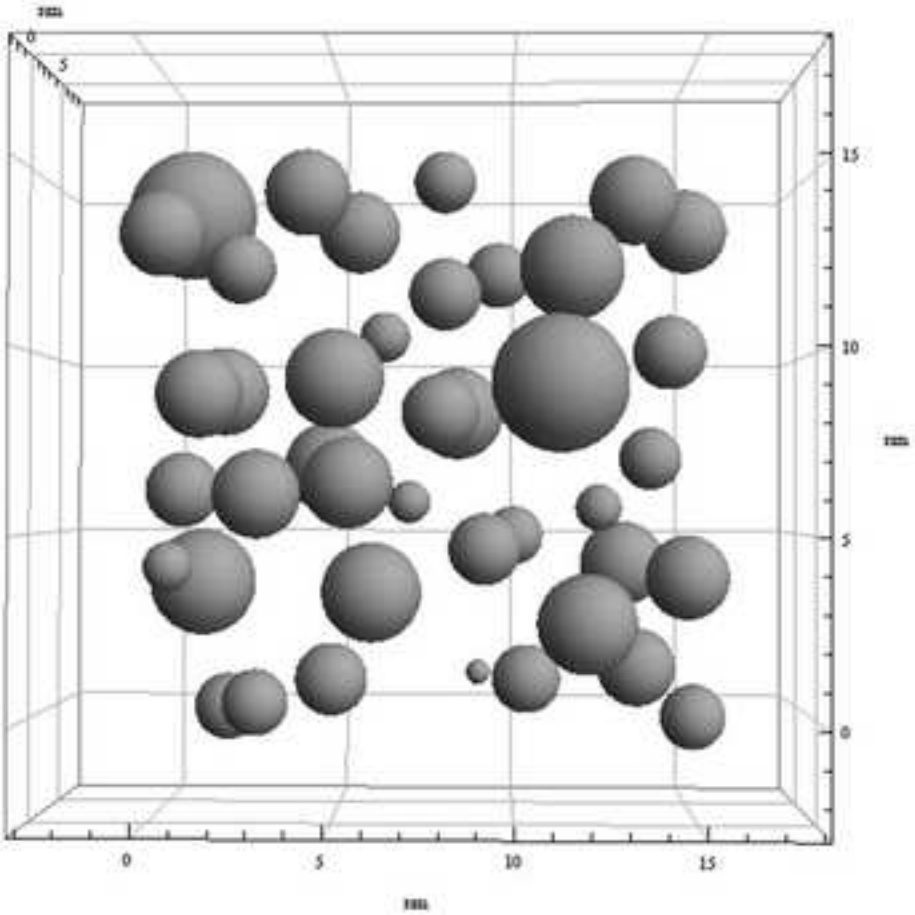

(b) a-C_Zr(4)

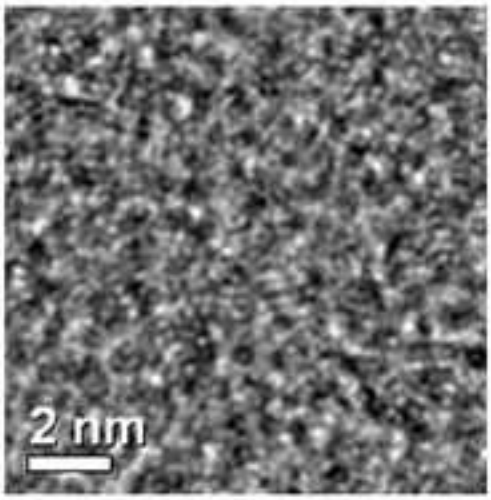

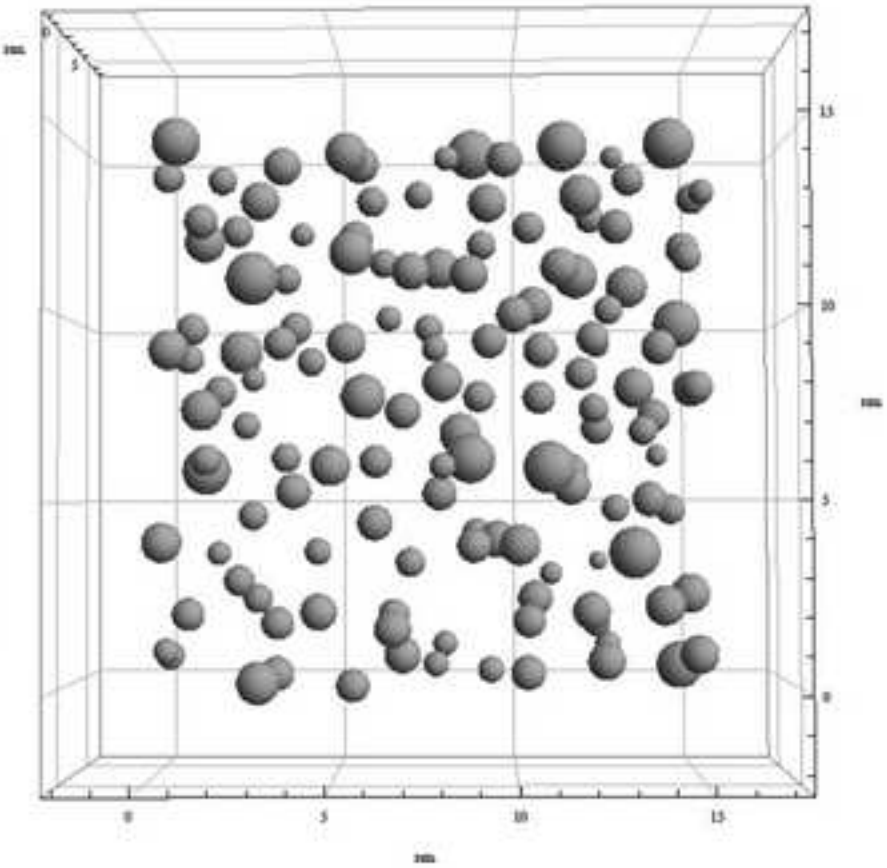

Figure6

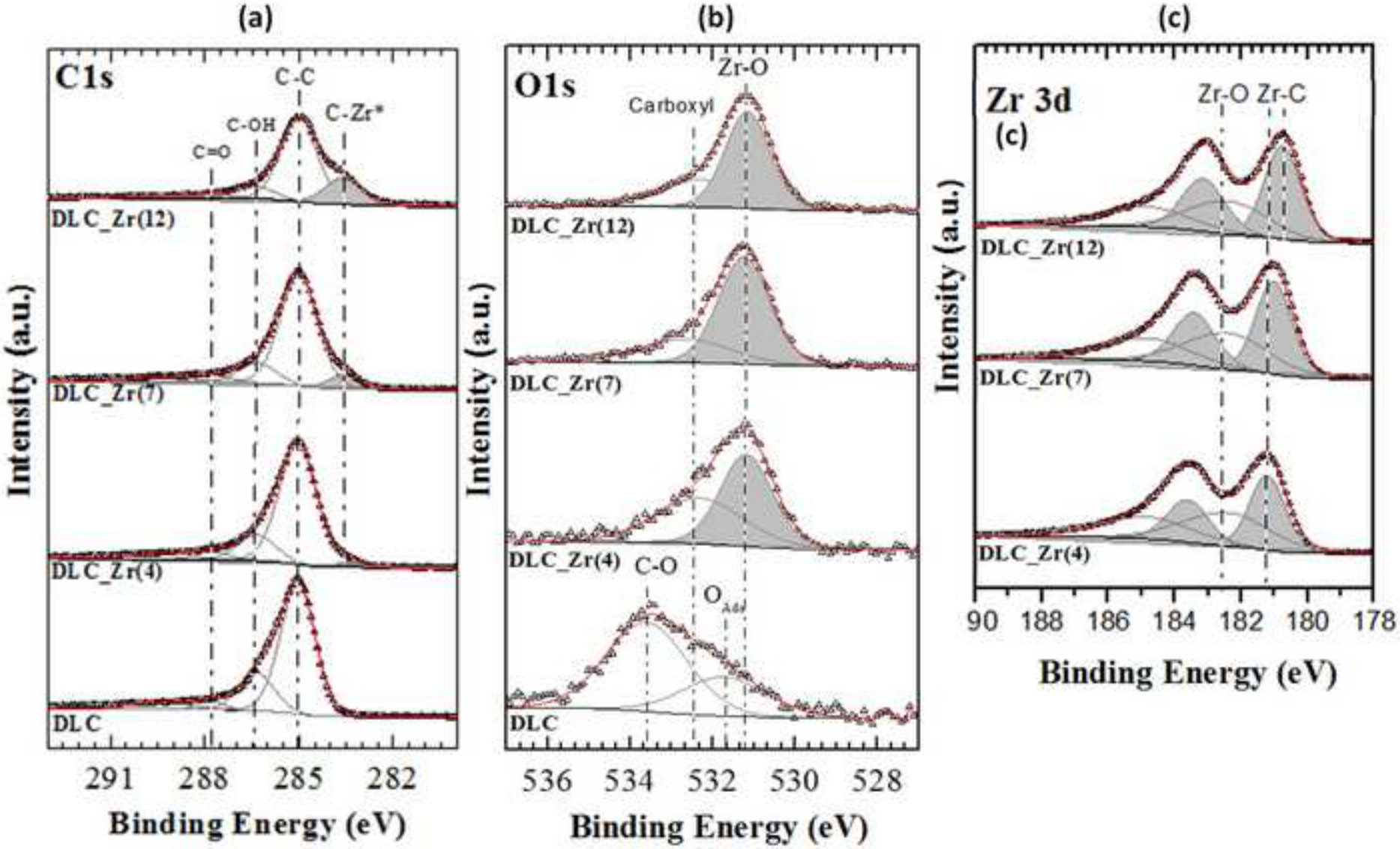
(a)
C1s
C-C
C-OH
C-Zr*
C=O
DLC_Zr(12)
DLC_Zr(7)
DLC_Zr(4)
DLC
Intensity (a.u.)
291
288
285
282
Binding Energy (eV)
(b)
O1s
Zr-O
Carboxyl
DLC_Zr(12)
DLC_Zr(7)
DLC_Zr(4)
C-O
O
DLC
Intensity (a.u.)
536
534
532
530
528
Binding Energy (eV)
(c)
Zr 3d
(c)
Zr-O
Zr-C
DLC_Zr(12)
DLC_Zr(7)
DLC_Zr(4)
Intensity (a.u.)
90
188
186
184
182
180
178
Binding Energy (eV)

List of figures

Figure 1 SEM micrographs showing the fractured cross-section of a-C, a-C_Zr(13) and a-C:H_Zr(10) films

Figure 2 AFM micrographs showing the topography of (a,b) a-C, (c,d) a-C_Zr(14) and (e,f) a-C:H_Zr(10) films deposited on Si wafers.

Figure 3 Cross-sectional TEM BF images of a-C_Zr(14) coating.

Figure 4 XRD diffractograms of (a) a-C_Zr(4), (b) a-C_Zr(7) and (c) a-C_Zr(14) films with selected patterns. The inset shows the fitted curve s of the peak phases present in the a-C_Zr(14) diffractogram, highlighting the ZrC phase (grey filling).

Figure 5 TEM BF images and particle distribution schematic representation of a-C_Zr(14) and a-C_Zr(4).

Figure 6 XPS (a) C1s, (b) O1s and (c) Zr 3d spectra for the non-hydrogenated films with different Zr contents after Ar^+ etching of the surface oxides.

List of Tables

Table 1 Coatings deposition parameters (A_{Zr}/A_C is the relative Zr pellets coverage of the erosion area,), chemical composition measured by XPS, deposition rate (Dep rate), thickness (t) and average roughness (Ra).

Table 2 Literature values on BE of the C1s, O1s and Zr 3d core-levels relevant for this study.

Table 3 XPS BE for the deconvolution of the peaks after Ar^+ sputtering

Table 4 Mechanical properties of the coating: compressive residual stress ($\sigma_{compressive}$), hardness (H), young modulus (E), H/E and H^3/E^2 ratios